Cellulose nanofibrils and nanocrystals in confined flow: Single-particle dynamics to collective alignment revealed through scanning small-angle x-ray scattering and numerical simulations

Tomas Rosén, Ruifu Wang, Chengbo Zhan, Hongrui He, Shirish Chodankar, and Benjamin S. Hsiao

Phys. Rev. E **101**, 032610 — Published 31 March 2020

DOI: 10.1103/PhysRevE.101.032610

Cellulose Nanofibrils and Nanocrystals in Confined Flow: Single Particle Dynamics to Collective Alignment Revealed through Scanning SAXS and Numerical Simulations

Tomas Rosén,[1,2,*] Ruifu Wang,[1] Chengbo Zhan,[1] Hongrui He,[1] Shirish Chodankar,[3] and Benjamin S. Hsiao[1]

[1] *Department of Chemistry, Stony Brook University, Stony Brook, New York 11794-3400, United States*

[2] *Treesearch, KTH Royal Institute of Technology, 10044 Stockholm, Sweden*

[3] *National Synchrotron Light Source II, Brookhaven National Lab, Upton, NY, USA*

(Dated: March 6, 2020)

Nanostructured materials made through flow-assisted assembly of proteinaceous or polymeric nanosized fibrillar building blocks are promising contenders for a family of new high-performance biocompatible materials in a wide variety of applications. Optimization of these processes relies on improving our knowledge of the physical mechanisms from nano- to macroscale and especially understanding the alignment of elongated nanoparticles in flows. Here, we study the full projected orientation distributions of cellulose nanocrystals (CNC) and nanofibrils (CNF) in confined flow using scanning microbeam SAXS. For CNC, we further compare with a simulated system of dilute Brownian ellipsoids, which agrees well at dilute concentrations. However, increasing CNC concentration to a semi-dilute regime results in locally arranged domains called tactoids, which aid in aligning the CNC at low shear rates, but limit alignment at higher rates. Similarly, shear alignment of CNF at semi-dilute conditions is also limited owing to probable bundle/flock formation of the highly entangled nanofibrils. This work provides a first quantitative comparison of full projected orientation distributions of elongated nanoparticles in confined flow and provides an important stepping stone towards predicting and controlling processes to create nanostructured materials on an industrial scale.

I. INTRODUCTION

Nature has a fascinating way of creating complex hierarchical structures, which have been tailored through millions of years of evolution to promote the survival depending on the local environment [1]. These intricate natural assemblies have inspired scientists to create similar nanostructured materials through self-assembly or forced assembly of nanosized particles, resulting in macroscopic materials with potentially tunable mechanical, optical and/or biological properties depending on nanoparticle arrangement [2, 3]. The processing of such materials on an industrial scale, relies on continuous structuring and assembly of nanoparticles in flowing systems. Regardless if the macroscopic material is one-dimensional (*e.g.* filaments or circuits [4–10]), two-dimensional (*e.g.* membranes, nanopapers [11–15]) or three-dimensional (*e.g.* 3D-printed materials [16–18]), the flow deformations during processing will affect the nanoparticle spatial and orientation distribution, and thus the final material properties. It is therefore crucial to understand the nanoparticle dynamics in process-relevant flow situations in order to control the process and possibly tailor the material properties through flow conditions.

A common way of stabilizing a nanoparticle dispersion is by introducing an electrostatic surface charge to the particles causing a repulsion and inhibiting the formation of aggregates occuring due to van der Waals attraction. At low (dilute) concentrations, thermal motion of the surrounding molecules will drive the particles towards randomness, *e.g.* towards a uniform spatial distribution through Brownian spatial diffusion and towards an isotropic orientation distribution through Brownian *rotary* diffusion. However, if the external deformation rate of the fluid is quick enough, the structure can be affected. At higher (semi-dilute) concentrations, the electrostatic interactions between particles will affect both the way they arrange due to external forcing as well as their Brownian diffusion.

Experimentally, the flow-behavior of nanoparticle dispersions is typically addressed through rheometry, by placing the dispersion in an ideal flow situation, such as the simple shear flow created by two parallel, opposite-moving walls [19–23]. The apparent viscosity is extracted by measuring the forces needed to shear the dispersion, which is affected by the nanoparticle spatial and orientation distribution. Rheometrical flows can be combined with structural characterization using *e.g.* small angle X-ray/Neutron scattering (SAXS/SANS) [20, 22–25], rheo-optical techniques with polarized light [19, 21, 26–28] or optical coherence tomography (OCT) [29, 30]. Since all methods have their advantages/disadvantages, a combination of *in situ* techniques could be used, where e.g. average alignment during flow is studied with SAXS while the time-dependent relaxation after stopping the flow is studied with rheo-optics as done by Rosén *et al.* [31].

The theory describing the motion of non-spherical, non-Brownian particles in linear velocity gradients dates back to early works by Jeffery [33]. The seminal works by

* trosen@kth.se

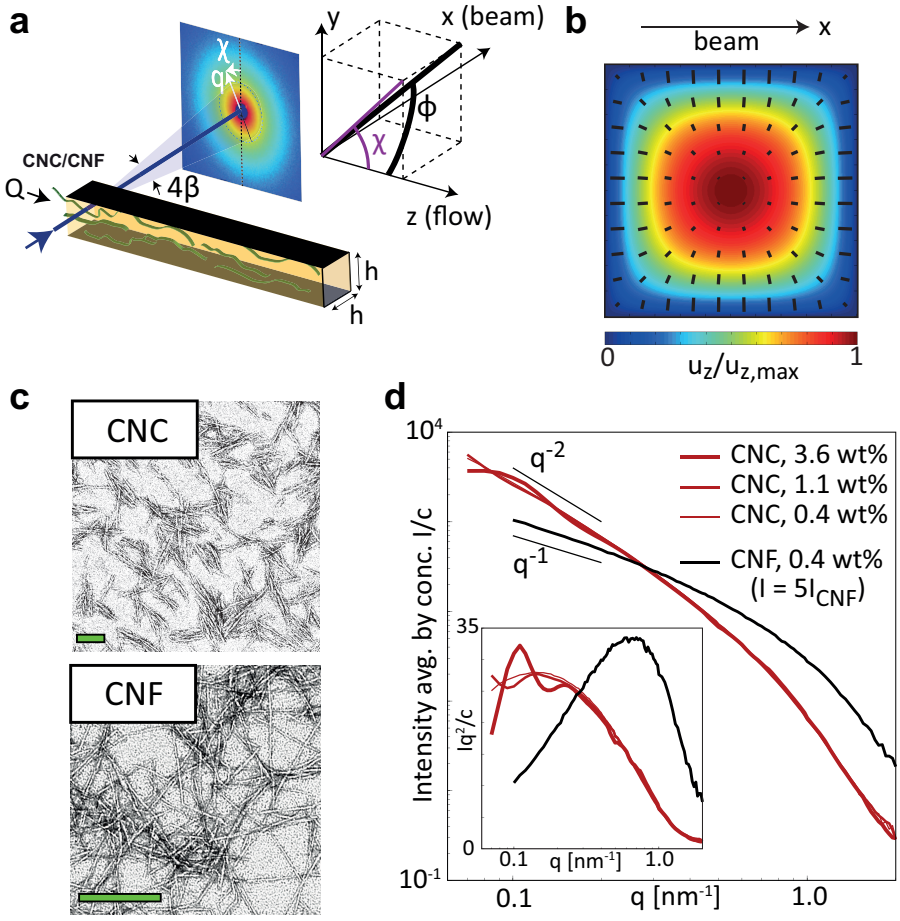

FIG. 1. Setup of the *in situ* SAXS experiment and characterization of the cellulose nanofibrils (CNF) and nanocrystals (CNC). (a) Schematic illustration of the flow used in this study. Dispersed CNF/CNC are flowing in a square channel flow (side $h = 1$ mm) with flow rate Q. The coordinate system is defined using x and z as the beam and flow directions, respectively. The 3D orientation of a particle to the z-axis is given by ϕ and the 2D orientation in the viewing (yz) plane is given by χ. The scattering intensity I is described on the SAXS-detector with polar angle χ and scattering vector $q = (4\pi/\lambda)\sin\beta$, with scattering angle 2β. Note that the angle χ in the detector plane is shifted 90° as the scattering from an elongated particle is perpendicular to its primary axis. (b) Analytical velocity profile in a square channel by Spiga and Morini [32]; the black lines indicate the shear direction with lengths scaled with shear rate. (c) TEM images of the CNF and CNC with the green scale bar indicating 250 nm. (d) Isotropic SAXS curves of the CNC and CNF dispersions used in this study (Lorentz-corrected curves Iq^2 vs q in inset figure).

Hinch and Leal [34–37] further described in great detail how Brownian motion affects the statistical distributions and rheology of dispersions with axi-symmetric ellipsoids, i.e. prolate and oblate spheroids. Generalizing the results to tri-axial ellipsoids, which are known to perform chaotic rotations in shear flow in the absence of Brownian motion [38], Almondo *et al.* [39] derived the appropriate Langevin equation and studied the effect of Brownian motion on these particles in linear flows. Numerical simulations of these equations can provide very valuable predictions of both orientation distributions and rheology of dilute suspensions of Brownian non-spherical particles, but often fall short when particle interactions become important at higher concentrations, which is especially relevant for nanofibrillar systems with very high particle aspect ratios. Although Brownian motion of systems with high aspect ratio macromolecules has been well described with the important Doi-Edwards theory [40, 41], our understanding of the thermal motion and angular dynamics of non-spherical nanoparticles in crowded environments is still incomplete [42, 43]. The key for developing these models is to have proper *in situ* characterization of orientation distributions and comparing with simulations with as little reduction in dimensionality as possible. As an example, the orientational distribution of tri-axial ellipsoids in flow is described in seven-dimensional space (three angles, three spatial coordinates plus time). With axi-symmetric particles and a developed flow situation with no gradients in flow direction, the system is reduced to four dimensions (two angles, two spatial coordinates; time-independent). Experimental characterization, such as SAXS/SANS, most often provides a projected repre-

sentation of the system, which reduces the dimensions to two (one projected angle and one spatial coordinate). A proper comparison with simulations should thus include the same reduction of the 4D system to 2D, and comparing the projected orientation distributions. However, often in these sort of studies, the data is reduced further through integration to a single alignment-dependent parameter before comparing. For example in previous studies using SAXS/SANS, there are a multiple definitions of anisotropy factors/orientation factors/order parameters based on the 2D azimuthal scattering profile [20, 24, 44, 45]. In other studies using rheo-optical techniques, the alignment is described similarly quantified using the degree of birefringence/retardance or dichroism [26, 28]. Consequently, the comparison of stationary orientation distributions between theory and experiments becomes more qualitative than quantitative, which leads to inaccurate models since there are an infinite number of distributions that can give rise to the same integrated order parameters.

In this work, we will try to address these issues and provide a framework for *quantitatively* study the flow of elongated nanoparticles with a combination of experiments and numerical simulations. We choose the simplest conceivable flow geometry relevant to material processes: a confined Poiseuille (developed/time-independent) flow through a straight quadratic channel (see Fig. 1a) with side $h = 1$ mm and flow rate Q, in which the dispersion is only subject to shear, but the shear directions and shear rates depend on the distance from the confining walls (see Fig. 1b). This flow geometry will represent the typical situation of a dispersion being pushed through pipes, tubing and nozzles in a realistic process. The experimental system will be elongated electrostatically stabilized nanoparticles derived directly from natural sources: cellulose nanocrystals (CNC) and nanofibrils (CNF). CNF and CNC have already been extensively studied [46–48] and further been demonstrated in continuous processes to align and assemble biobased nanostuctured materials where the orientation distribution is directly linked to mechanical properties of the final product [6, 10, 49].

Firstly, we will describe how to obtain the projected 2D orientation distributions of dispersed CNF and CNC in the square channel using *in situ* scanning microbeam SAXS [50–54]. Secondly, we will use the Langevin equation by Almondo [39] to predict the 4D orientation distributions of dilute ellipsoids in this flow, and describe how to reduce the data to obtain the same 2D distributions as in the experiments. Using this framework, we will address the following questions:

1. Can dilute CNC be modeled as dilute Brownian ellipsoids?
2. In systems of CNF and CNC at process-relevant concentrations, how does the behavior differ from systems of dilute Brownian ellipsoids?

Finally, since the average orientation of the crystalline cellulose material also affects its birefringence, we will demonstrate how a simple and cheap rheo-optical experiment can provide some quantitative measurements of flow-induced alignment that can be compared with both SAXS and simulations.

II. MATERIALS AND METHODS

A. Sample characterization and flow setup

Dispersions of CNF and CNC are prepared from commercially available nanocellulosic slurrys purchased from the University of Maine Process Development Center (see appendix A for details). The dimensions of CNF were estimated through transmission electron microscopy (TEM) and they were fairly polydisperse with lengths between 200-1000 nm and widths of 3-5 nm (see Fig. 1c). The aspect ratios (length/width) thus is of the order of r_p = 50-300. The thicker (around 10-30 nm wide) and stiffer CNCs were found to have aspect ratios around r_p = 10-20. The systems were initially prepared at concentrations of 0.4 wt%, which was similar to what previously has been used during flow-assisted assembly of CNF [10, 44]. Given the differences in aspect ratios, the CNF dispersion could be considered semi-dilute at this concentration, while the CNC dispersion was dilute (based on crowding factor, see appendix A for details). In order to also study CNC up to semi-dilute conditions, dispersions were prepared at 1.1 wt% and 3.6 wt%. At the highest concentration used here, the CNC is known to arrange locally into *tactoids*; highly ordered regions with CNC, which are isotropically distributed in the sample in the absence of external forces [48, 55–57]. Due to the slenderness of the CNF, it is very difficult to reach truly dilute conditions as the required concentration needs to be lower than approximately 0.02 wt%. Any experimental characterization with SAXS at these concentrations is practically impossible due to the low difference in electron density between cellulose and water. Therefore, CNF is only studied at semi-dilute concentrations.

B. *In situ* SAXS experiments

The experimental flow cell consisted of a 1 mm aluminum plate with a milled 1 mm wide channel sandwiched between two Kapton films (DuPont, 200HN, each 51 μm thickness), serving as both walls and window material. The entire cell is mounted with two outer aluminum plates for mechanical stability and fluid distribution. Details and illustration of the experimental flow cell is provided in appendix B.

The *in situ* SAXS experiments were performed at the LiX beamline (16-ID) in NSLS-II at Brookhaven National Laboratory, USA. The measurements were performed in transmission geometry through the flow cell, which was mounted on a translational stage that allowed the beam position to be controlled in y-z direction. The

chosen X-ray wavelength was $\lambda = 0.79$ Å and the sample-detector-distance was 4.3 m. The beam size was estimated to be 50×50 μm^2 and the SAXS scattering patterns were recorded on a Pilatus 1M detector with pixel size 172×172 μm^2. The detector images were converted into diffractograms with polar coordinates $I(q, \chi)$, using scattering vector $q = (4\pi/\lambda) \sin \beta$ (2β is the scattering angle) and azimuthal angle in the detector plane χ. Since the scattering from an elongated particle is perpendicular to its orientation, the angle χ is defined to be zero perpendicular to flow direction ($q_z = 0$). Background scattering was obtained by flowing only DI water through the channel and was removed from all diffractograms of the flowing CNC/CNF dispersions.

The SAXS diffractogram is a representation of the Fourier-transformed electron density distribution in the sample giving a statistical description of structures at length scales $L = 2\pi/q$. Since the length of the nanoparticles is much greater than the minimum measurable q, the scattering here is completely dominated by the CNF/CNC cross-sections.

1. *Isotropic SAXS – cross-sectional dimensions*

Running the system at very low flow rates, there is very little induced alignment and the scattering curves $I(q)$ are independent of χ. These curves are shown in Fig. 1d. The scattering pattern of the CNF dispersion has a $I \propto q^{-1}$ asymptote at low q, which is indicative of a slender rod-like system. The mean cross-sectional dimensions were found to be 5.6×2.0 nm^2 using a monodisperse parallelepiped model fit (assuming very slender fibers) to the scattering data. The dilute CNC dispersion exhibited a higher slope at low q closer to $I \propto q^{-2}$ indicative of flat objects. However, a $I \propto q^{-1}$ asymptote should typically be found at smaller angles than what could be obtained in the present experiments [58]. A polydisperse parallelepiped model fitting of the dilute CNC data revealed mean cross-sectional dimensions of 30.8×3.5 nm^2. The CNC particles are thus highly tri-axial with width dimensions consistent with TEM images. At higher concentrations, the transition to the tactoidal state is observed through the emergence of the structure peak at $q_{\text{peak}} \approx 0.1$ nm^{-1} for the 3.6 wt% CNC dispersion. This peak corresponds to the high order within the tactoids [59, 60] where the approximate inter-particle distance of $d = 2\pi/q_{\text{peak}} \approx 63$ nm is determined. The details of the fitting procedure is provided in appendix C.

2. *Anisotropic SAXS – orientation distributions*

During flow, the scattering pattern becomes anisotropic and dependent on χ. The normalized azimuthal scattering intensity $I_{\text{norm}}(\chi)$ averaged over q-values corresponding to length scales between the minor and major particle dimensions corresponds to the orientation distribution function (ODF) $I_{\text{norm}}(\chi) = \Psi_\chi$, i.e. the experimentally determined probability distribution of the CNF/CNC projected angle χ [45].

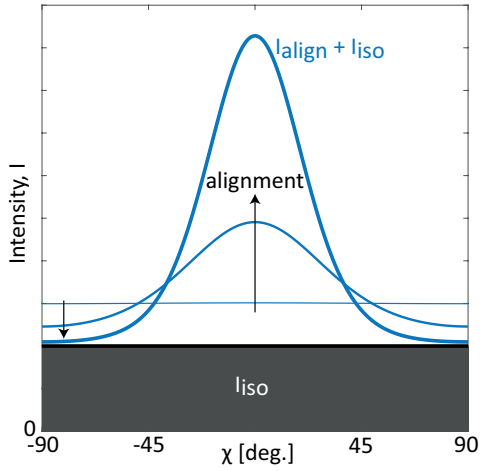

FIG. 2. Schematic illustration of the azimuthal intensity profile from a SAXS experiment at a certain q with different degrees of alignment. The intensity is assumed to be the sum of an isotropic part I_{iso} and an aligned part I_{align}. With an aligned reference, I_{iso} can be estimated as $I_{\text{iso}} \approx I(q, \chi = 90°)$. The distribution of the projected angle Ψ_χ is obtained by normalizing I_{align}.

The typical dispersions from nanocellulose are rarely only containing the long CNF/CNC described earlier, but also shorter residual particles being subject to very fast Brownian rotary diffusion with an orientation distribution that stays isotropic over all flow rates [43]. There can also be residual particles which are nearly spherical and can not be aligned with reasonable hydrodynamic forces. The overall scattering pattern can thus be seen as the sum of an aligned part and an isotropic part $I(q, \chi) = I_{\text{align}}(q, \chi) + I_{\text{iso}}(q)$, as schematically explained in Fig. 2. By having a highly aligned reference of the CNF/CNC dispersion [31, 44], the isotropic contribution can be set as $I_{\text{iso}}(q) = I(q, \chi = 90°)$, i.e. as the scattering in z-direction. Since already at fairly moderate degrees of flow-alignment, the probability of particles in cross-streamwise direction is almost zero, the system does not need to be close to perfect alignment for a correct estimation. A demonstration of this procedure using simulated SAXS patterns from systems with a predefined ODF is provided as supplementary material.

In order to accurately find $I_{\text{iso}}(q)$, the experimental flow cell was designed with a flow-focusing section, where the dispersion could be aligned with strong extensional flow (see Fig. 3a). The isotropic contribution is set where both core and sheath flows have a rate of $Q = 200$ ml/h and taken at position $x/h = 0$ and $z/h = 1.5h$, where the highest alignment was found (Position 6 in figure). Having determined I_{iso}, the experimental 2D ODF Ψ_χ at other positions in the channel was obtained by normalizing $I_{\text{align}}(q, \chi) = I(q, \chi) - I_{\text{iso}}(q)$ at a certain q through (with χ in radians):

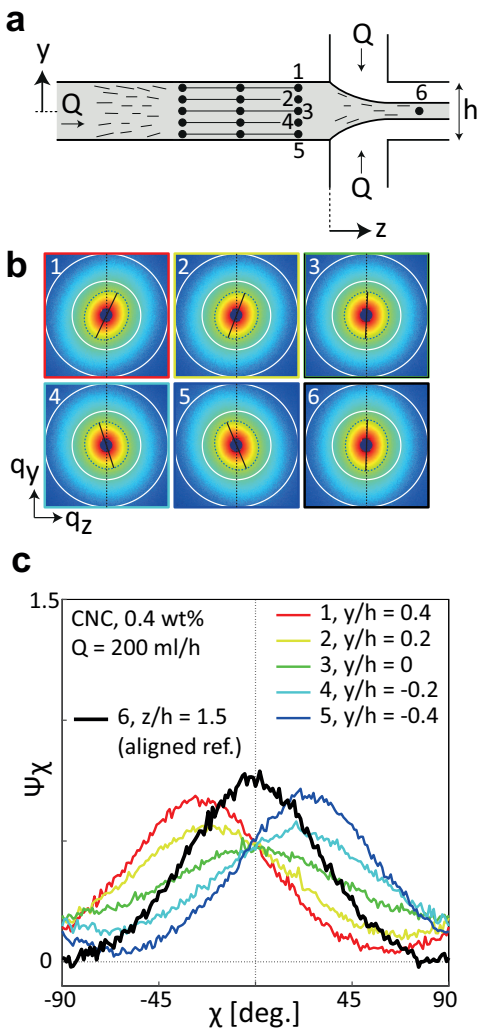

FIG. 3. Illustration of the SAXS experiments to obtain the 2D ODF Ψ_χ for dilute CNC (0.4 wt%) at $Q = 200$ ml/h. (a) Schematic illustration of the flow-focusing channel, where 5 channel heights (1-5) are considered upstream of the focusing region. Position 6 (at z/h=1.5) is corresponding to the position used as a high-aligned reference position. (b) SAXS diffractograms obtained at positions 1-6. The white circles indicate the range $q \in [0.25, 0.45]$ nm^{-1} used to evaluate the ODF and the dashed ellipse indicate the iso-contour of the intensity (with black line indicating ellipse major axis). (c) The corresponding 2D ODF Ψ_χ at the same positions and conditions.

$$\int_{-\pi/2}^{\pi/2} I_{\text{align}}(q,\chi)d\chi = 1 \tag{1}$$

and averaging I_{align} in the range $q \in [0.25, 0.45]$ nm^{-1}. Note that in this region, the scattering is not affected by the structure contribution even at the higher CNC concentration (Fig. 1d).

Examples of the scattering patterns and the resulting 2D ODFs Ψ_χ of dilute CNC at $Q = 200$ ml/h at 5 different channel heights ($y/h = -0.4, 0.2, 0, 0.2$ and 0.4) averaged over three z-locations are illustrated in Fig. 3b-c.

As expected, highest degree of alignment is found close to the visible walls, since the average shear along the beam path is the greatest (cf. Fig. 1c). The tilted distribution indicates an average orientation pointing slightly towards the channel center, i.e. in the shear-direction, which is expected from a system of Brownian particles [61, 62]. The reason for this tilted distribution originates from the orientation probability being enhanced along the shear flow's extensional axis (45° between flow and velocity gradient directions), where the (non-Brownian) Jeffery orbits have negative divergence, and suppressed in the compressional axis (−45° between flow and velocity gradient directions) where Jeffery orbits have positive divergence [61].

C. Numerical simulations

The ideal orientation distributions of dilute Brownian ellipsoids in a square channel flow were obtained using numerical simulations. The details about the procedure is given in appendix D. In brief, the simulation relies on the single particle moving along a single streamline in the flow, neglecting any translational diffusion. With this assumption, since the channel flow consists of straight streamlines, the single particle is always subject to the same velocity gradient during its motion. Therefore, the particle rotation can be simulated in a Lagrangian frame on the streamline using the derived Langevin equation by Almondo *et al.* [39]. The procedure is illustrated in Fig. 4. Four different spheroidal sizes were chosen for this study (Fig. 4a), where the particle minor axis is fixed at 10 nm, closely matching the cross-sectional area with the CNC as obtained from the isotropic SAXS analysis (triaxiality of the Brownian ellipsoids has little effect on the ODF [39]). The major axis was varied to obtain aspect ratios (major/minor axis) $r_p = 10, 15, 25$ and 50.

In this simulation, the square channel cross-section was divided into 10×10 cells (Fig. 4b). In each cell, the velocity gradient matrix $\mathbb{J}$ was estimated using the analytical velocity profile in a laminar square channel flow by Spiga and Morini [32]. The other simulation conditions involved the use of temperature $T = 293$ K and a fluid with kinematic viscosity of water.

A number of spheroids of a certain r_p were simulated in a given cell to form the average 3D orientation distribution function (ODF) in the cell. The simulations were then performed by varying the aspect ratio r_p and flow rate Q. The average 3D ODF at a given channel height $y/h = -0.4, 0.2, 0, 0.2$ and 0.4 was taken as the average of all adjacent cells in the viewing direction x (Fig. 4c). Finally, the average 3D ODF was projected on the viewing (yz) plane, in order to obtain the 2D ODF of the particles, *i.e.* the distribution Ψ_χ of the projected angle χ in the viewing plane (Fig. 4d). Since Ψ_χ can

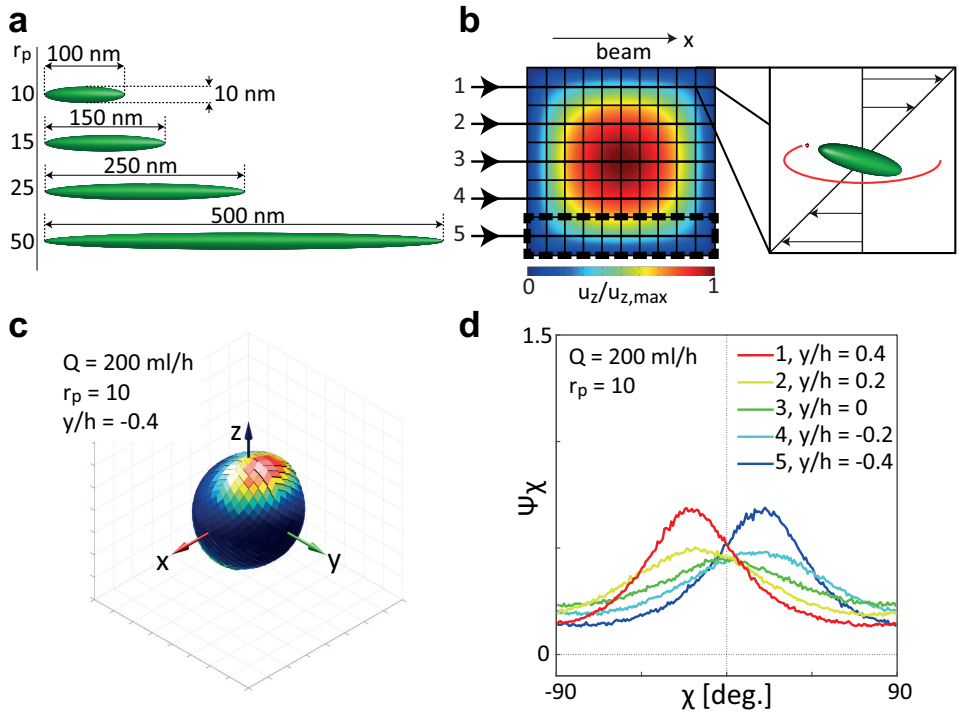

FIG. 4. Illustration of the numerical procedure to obtain 2D ODF Ψ_χ. (a) Four different sized spheroids with same width of 10 nm with aspect ratios (major/minor axis) $r_p = 10, 15, 25$ and 50 are considered. (b) Five different channel heights y (1-5) are considered. The cross section of a fully developed laminar channel flow is divided into 10×10 cells, in which the velocity gradient is estimated and used to simulate the motion of a single Brownian spheroid. (c) A 3D spherical histogram illustrating the 3D ODF at $y/h = -0.4$ is obtained as the average over many particles in each of the 20 adjacent cells at a certain channel height, marked with dashed box in (b), and subsequent averaging over these cells. (d) Projecting the orientations on the viewing (yz) plane, the 2D ODF Ψ_χ is obtained.

also be obtained using SAXS, this 2D ODF can be directly compared with the experiments [45]. Since the 3D ODF is not axi-symmetric (Fig. 4c), it is not possible to reconstruct it from Ψ_χ [45].

Just as in the SAXS-experiments, the alignment is the highest near the visible wall (at $|y/h| = 0.4$) and the ODFs have a clear mean orientation towards the center of the channel as expected.

III. RESULTS

In order to compare the orientation distributions at different flow conditions, two parameters are extracted that describe the ODF at $|y/h| = 0.4$. The most probable projected orientation $\chi_{\max}$ is found through a spline fit of the data, and the orientation in this direction is given by the 2D order parameter $S_{\chi-\chi_{\max}} = \langle 2\cos^2(\chi - \chi_{\max}) - 1 \rangle$ (note that the ordinary 3D order parameter using the second Legendre polynomial, sometimes called the *Hermans orientation factor*, is not appropriate here as the system lacks axi-symmetry [45]).

A. Dilute CNC versus Brownian ellipsoids

The projected ODFs Ψ_χ from the numerical simulations are plotted at different channel heights $y/h = -0.4, -0.2$ and 0 (called *wall*, *intermediate* and *center* regions) in Fig. 5 for different aspect ratios r_p and flow rates $Q = 100$ and 200. These are in turn compared with the experimental ODFs Ψ_χ of the dilute CNC (0.4 wt%). The data of both wall region locations $|y/h| = 0.4$ is summarized in terms of angle $\chi_{\max}$ and alignment $S_{\chi-\chi_{\max}}$ in Fig. 6.

For the dilute ellipsoids, there is a strong dependency of the ODFs, where the shear-induced flow alignment is increasing rapidly with respect to both aspect ratio and flow rate as hydrodynamic forces overcome Brownian motion. The increased flow alignment is a consequence both of the ODF becoming more centered around the flow direction as $\chi_{\max} \to 0$ and higher alignment in this direction. The same trend is seen at all channel heights y/h, where as mentioned before, the strongest alignment is found close to the visible walls ($|y/h| = 0.4$). Furthermore, it is noted that the projected ODFs scale almost linearly with the ellipsoid aspect ratio and flow rate, i.e. the ODFs look very similar when doubling the flow rate from $Q = 100$ to 200 ml/h for half the aspect ratio

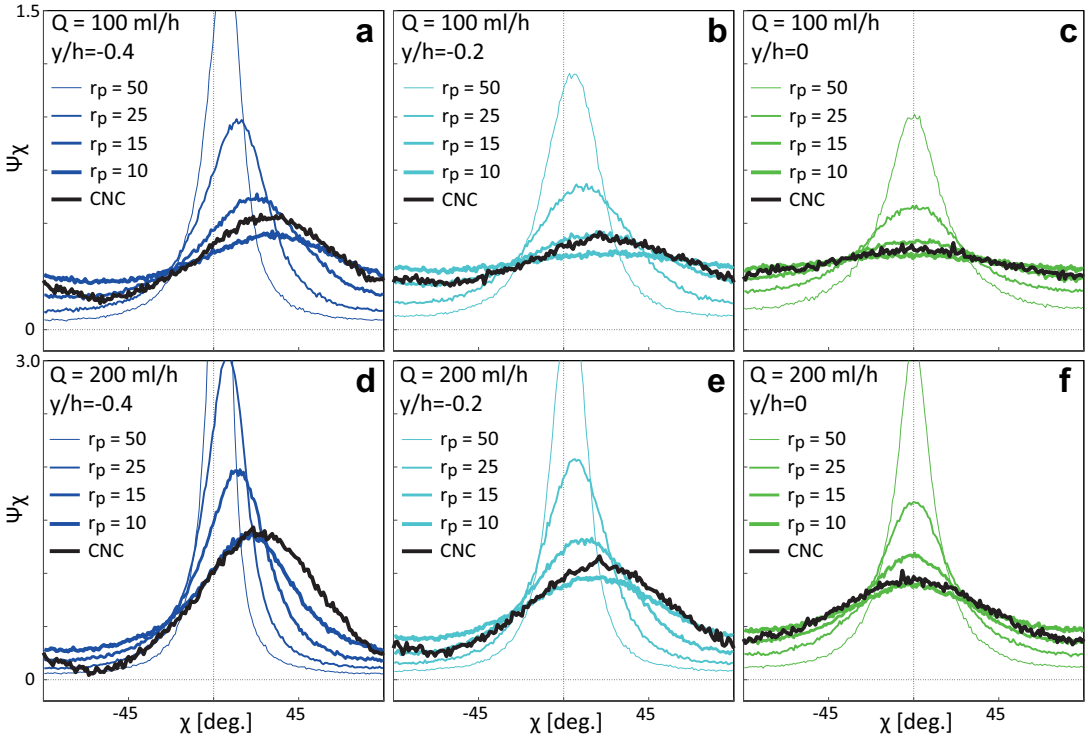

FIG. 5. Projected ODFs Ψ_χ of dilute Brownian ellipsoids of different aspect ratios r_p compared with dilute CNC (0.4 wt%). The flow rate is $Q = 100$ ml/h in (a)-(c) and $Q = 200$ ml/h in (d)-(f). The ODFs are plotted for (a)&(d) the wall region ($y/h = -0.4$); (b)&(e) the intermediate region ($y/h = -0.2$) and (c)&(f) the center region ($y = 0$).

r_p, e.g. reducing r_p from 50 to 25 or from 25 to 15.

The projected ODFs of dilute CNC follow very closely the ODFs of Brownian ellipsoids between $r_p = 10$ and 15. Just like these short ellipsoids, the CNC ODFs are almost isotropic at $Q = 100$ ml/h in the center region (Fig. 5c), and have almost an identical shape in both the center and intermediate regions up to $Q = 200$ ml/h. Although the averaged alignment in the wall region is very similar to the Brownian ellipsoids between $r_p = 10$ and 15 (see Fig 6b), there are some differences in the ODF shape. The peak of the CNC ODF is broader, which also results in the angle $\chi_{\max}$ not following the trend of the simulated system in Fig 6a.

B. Semi-dilute CNC and CNF

In Fig. 7, the projected ODFs Ψ_χ are plotted in the same way as before for CNC at three different concentrations from dilute (0.4 wt%) to semi-dilute/tactoidal (3.6 wt%). These are compared with CNF at semi-dilute conditions (0.4 wt%). The angle $\chi_{\max}$ and alignment $S_{\chi-\chi_{\max}}$ in the wall regions are further summarized in Fig 8.

For CNC, there is very little happening to the ODFs going from 0.4 to 1.1 wt% in either part of the channel. However, the flow alignment is slightly higher with both a reduction of $\chi_{\max}$ and $S_{\chi-\chi_{max}}$ in the wall region. The electrostatic interactions giving rise to the appearance of structure in Fig. 1d thus also aid in aligning the system in shear, which could be modeled fairly well as a system with dilute ellipsoids with less Brownian particles (higher r_p; cf. Fig. 6). As the CNC dispersion enters the tactoidal state at 3.6 wt%, there is a dramatic change of the ODF shapes in the channel. Already at low flow rates, the system quickly aligns and reaches much higher values of $S_{\chi-\chi_{max}}$ in the wall region than what is found for the less concentrated CNC (Fig. 8). Increasing the flow rate, it is clear that the ODF shape is sharpening slightly (Fig. 7), but remains almost the same with almost constant alignment $S_{\chi-\chi_{max}}$ and angle $\chi_{\max}$ when increasing flow rate from $Q = 100$ to 200 ml/h (Fig. 8). Furthermore, compared to the dilute CNC, the alignment is also varying less between center and wall regions (see inset in Fig. 8b), illustrating a system that is seemingly independent of average shear rates. At the walls, the alignment of dilute CNC is even likely to be exceeding that of the tactoidal state at flow rates $Q > 200$ ml/h.

Interestingly, the semi-dilute CNF shows significant similarities with the semi-dilute/tactoidal CNC in terms of the way they align in the square channel. Although not reaching the same high levels of alignment as the CNC system, the CNF also align easily at low flow rates. As the flow rates increase, the ODF only changes slightly with almost constant $\chi_{\max}$ in the wall region as well as almost constant alignment $S_{\chi-\chi_{max}}$ at different channel

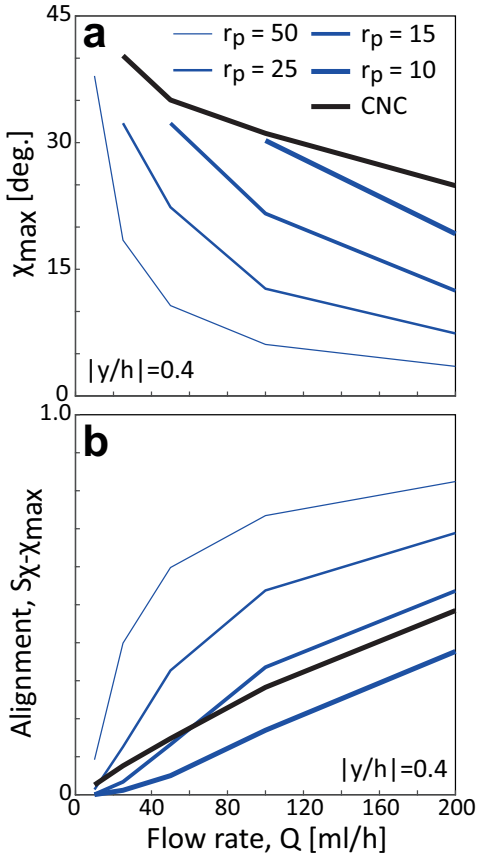

FIG. 6. Results from *in situ* SAXS of dilute CNC (0.4 wt%) and numerical simulations of Brownian ellipsoids with different aspect ratio r_p in the wall region of the channel $|y/h| = 0.4$. (a) Maximum probable angle $\chi_{\max}$. (b) Alignment $S_{\chi-\chi_{max}}$ in the $\chi_{\max}$-direction.

heights and flow rates.

IV. DISCUSSION

The results in the previous section highlights two important findings:

1. The simulated projected ODFs of Brownian ellipsoids with similar dimensions as CNC match very well with the measured projected ODFs of dilute CNC. The subtle differences of the ODF shape in the wall region is probably due to all the strict assumptions in the simulations including particles following exact straight streamlines and not interacting either with each other or with the wall, something that might be more questionable at higher flow rates.

2. Semi-dilute systems of CNF and CNC behave very different from dilute systems, where they align easily at low flow rates but the ODF remains more or less constant when increasing flow rate.

Although it is very difficult to prove exactly what is giving rise to these nanostructural changes due to particle interactions, we will here present a couple of hypotheses based on previous findings on similar systems.

Firstly, we must address the fact that semi-dilute CNF/CNC dispersions are non-Newtonian and are typically shear-thinning [17, 63]. This means that the velocity profile in a pipe (or square channel) becomes less parabolic and have stronger shear layers at the wall and less shear (near-plug flow) in the center. However, for similar CNF suspensions used here, it has previously been shown that this effect is small [30]. Also the non-Newtonian effects of the CNC dispersion at 3.6 wt% is also small [64]. Apart from these previous studies, the data in the present study is not favoring the idea of a plug-like core, as this likely would result in a large difference in projected alignment between center and wall-regions, which is opposite to observations in Fig. 8b. We therefore assume that the velocity profile of semi-dilute CNF/CNC also is close to the analytical laminar profile.

For CNC dispersions, a hypothesized scenario is illustrated schematically in Fig. 9. The region outside the particle that is affected by its electrostatic charge is described by the Debye length. At dilute conditions, the average distance between the particles is much greater than the Debye length and the particles behave similar to Brownian ellipsoids (Fig. 9a). At semi-dilute state, the CNC arrange in locally ordered tactoids where the particles are close enough to always affect each other through electrostatic interactions (Fig. 9b) [55, 57]. When shearing the system at low rates, the domains of locally ordered particles move collectively and the influence of Brownian motion from surrounding molecules is suppressed. This is very similar to the effect noted by De France *et al.* [57], who observed that a magnetic field could slowly align CNC, but only at concentrations corresponding to a tactoidal state, as lower concentrations would be subject to too strong Brownian motion.

At higher shear rates, there are several effects that can limit the degree of alignment of CNC in concentrated dispersions.

Our proposed hypothesis is that the CNC are approximately moving along with the tactoid according to the non-Brownian Jeffery-orbit [33] corresponding to the tactoid shape. The tactoids are sometimes displayed as nearly-spherical objects [56], which of course will not yield very high alignment since a sphere just rotates with constant angular velocity in shear. Assuming that the the aspect ratio of a tactoid is lower than that of an individual nanocrystal particle, the maximum degree of alignment will be limited due to the Jeffery-period being shorter and the tactoid spending less time with its main axis aligned in flow-direction. The average ODF of non-Brownian Jeffery-orbits from an initially random system is also independent of shear rates, which would explain the low difference in alignment between center and wall-regions. Assuming further that the average alignment of CNCs inside the tactoid is tilted with respect to the

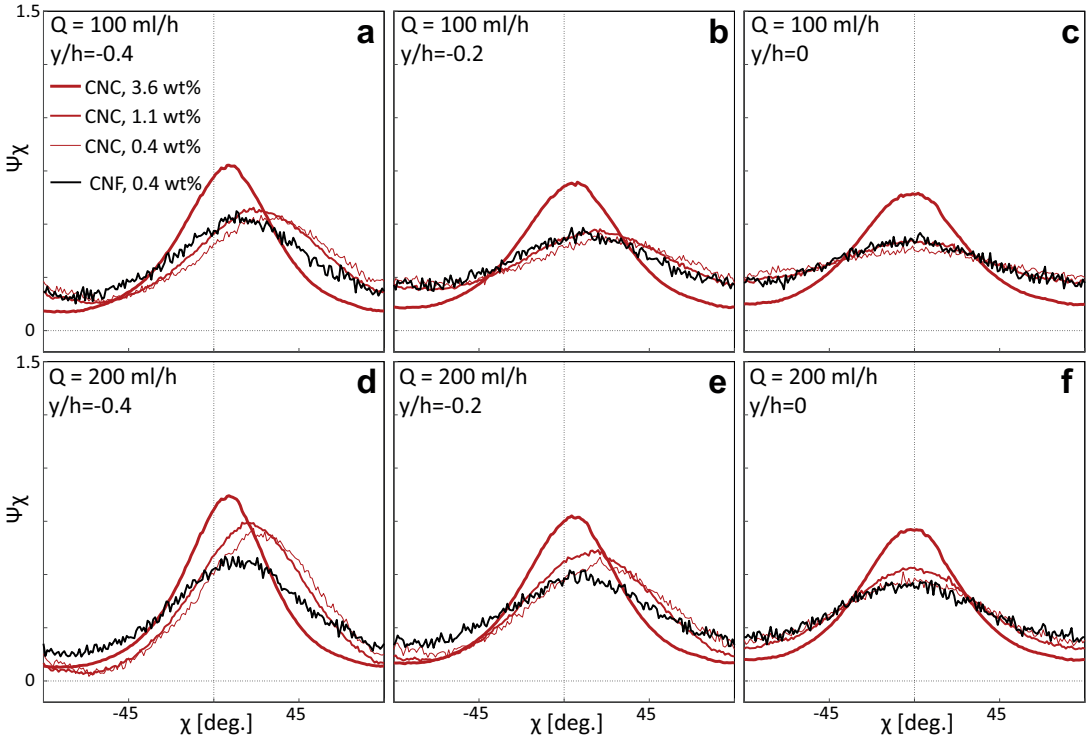

FIG. 7. Projected ODFs Ψ_χ of CNC at various concentrations compared with CNF (0.4 wt%). The flow rate is $Q = 100$ ml/h in (a)-(c) and $Q = 200$ ml/h in (d)-(f). The ODFs are plotted for (a)&(d) the wall region ($y/h = -0.4$); (b)&(e) the intermediate region ($y/h = -0.2$) and (c)&(f) the center region ($y = 0$).

tactoid major axis as illustrated in Fig. 9b, would be a possible explanation for the tilt angle at the wall not approaching zero with increasing flow rate.

An alternate hypothesis could be that shearing forces might become so strong that the local arrangement is disturbed and particles can move individually. The collisions of rod-like Brownian particles is known to enhance the thermal noise as they provide more "kicks" to each other, thus resulting in stronger Brownian rotary diffusion [65]. However, this hypothesis would imply that the structure peak will be affected with higher shear rates. Fig. 10 shows the Lorentz-corrected scattering intensities in flow (z) and cross-flow (y) directions in the wall region ($|y/h| = 0.4$) at two different flow rates $Q = 10$ and 200 ml/h. It is clear that the scattering curves maintain more or less the same shape with increasing shear rate and only change in absolute intensity following the higher scattering anisotropy due to alignment. Therefore, we can conclude that the tactoidal structure is not disrupted by the increasing shear.

Another alternate hypothesis could relate to the fact that the nematic equilibrium arrangement of CNC consists of domains of particles, not perfectly aligned with nearby domains, but having a pitch resulting in a chiral structure [47, 59, 66]. Since the perfect alignment would result in a zero pitch, there could be electrostatic torques that counteract the hydrodynamic alignment. However, this effect is probably very small as it has been shown previously that the pitch disappears when shear is applied [48, 66] and reappears when shearing is removed.

For CNF dispersions, similar trends are found as for the semi-dilute CNC system; both tilt angle and alignment are nearly constant in the shear layers of the channel with increasing flow rate. The alignment is still relatively high at low flow rates, which probably again is due to the collective motion of the loosely entangled fibrils. The collective motion is believed to be mechanically induced due to entanglement rather than through electrostatic interactions, since the average distance between fibril segments is much greater than the Debye length, which is of the order of 10 nm for CNF [43]. At higher shear rates, there can also be several reasons for the limiting behavior, *i.e.* that a high degree of alignment can not be reached in the shear layers, which is schematically illustrated in Fig. 11.

One possibility is that the nanofibrils are slightly flexible, which could cause the particle to curl up in the shear flow and self-entangle into almost isotropic bundles that rotate with the local vorticity (Fig. 11a), something that is known to happen for macroscopic flexible fibers [67, 68] and polymers [69]. Even if the nanofibrils would be rather stiff, the intermittent tumbling motion of elongated particles in shear could lead to mechanical interactions with other fibrils that make them form larger bundles or flocks rotating with vorticity (Fig. 11b), something that has also been seen in both CNF and CNT

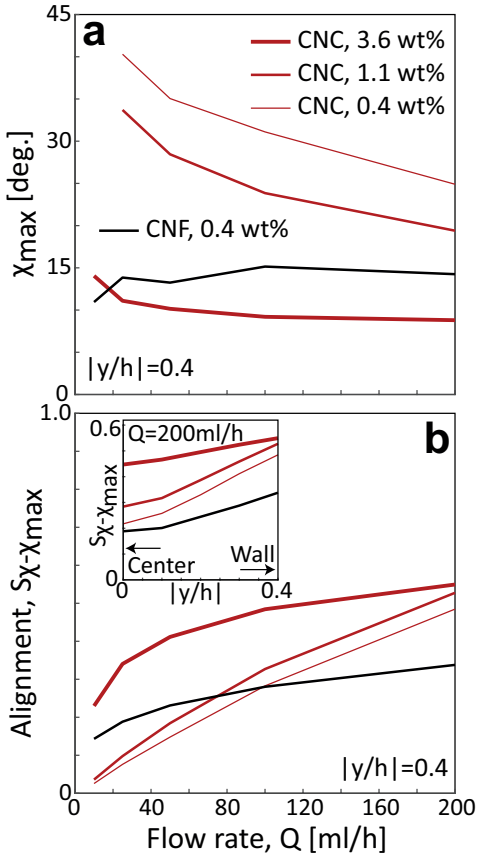

FIG. 8. Summarized results from *in situ* SAXS of CNC at various concentrations compared with semi-dilute CNF. (a) Angle $\chi_{\max}$ and (b) Alignment $S_{\chi-\chi_{max}}$ in the wall region $|y/h| = 0.4$. The inset figure shows the alignment distribution $S_{\chi-\chi_{max}}$ depending on channel height y/h at $Q = 200$ ml/h.

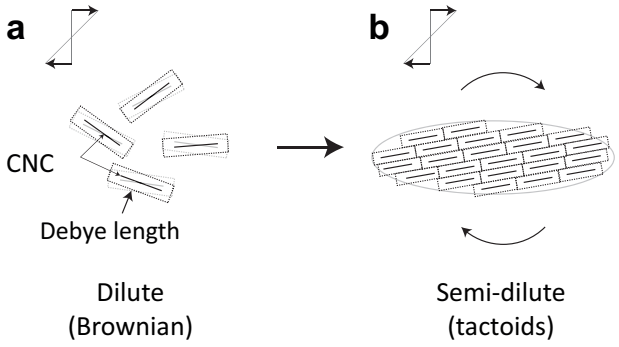

FIG. 9. Schematic illustration of hypothesized CNC interactions. (a) In dilute state, the Debye length is much smaller than distances between particles and CNC behave like Brownian ellipsoids. (b) In semi-dilute state at low shear rates, the CNC are influencing each other with electrostatic forces and moving collectively in less Brownian *tactoids*.

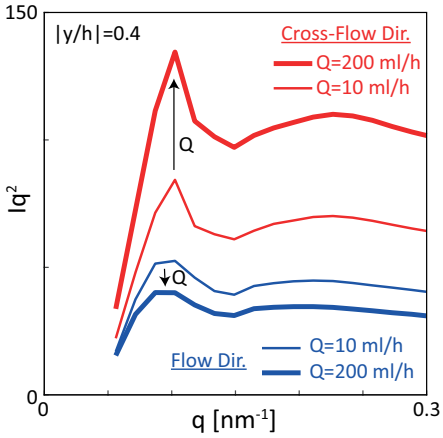

FIG. 10. Lorentz-corrected intensities Iq^2 versus q evaluated in flow (z) direction and cross-flow (y) direction in the wall region $|y/h| = 0.4$ at $Q = 10$ and 200 ml/h.

dispersions [24, 25, 29]. It is also likely that these flocks are slightly stretched towards the extensional direction of the shear flow (45° w.r.t. flow direction) as known for deformable capsules [70] and red blood cells [71]. This would make the fibers having a preferred alignment in the stretching directions. The increased alignment at higher shear rate could be due to further stretching of these potentially elastic aggregates. Martoïa *et al.* [72] argued that the Brownian rotary diffusion should have a negligible effect on the CNF dispersions in shear flow, which is consistent with the observed constant ODF over all flow rates here. However, flow-stop experiments of similar systems shows both fast and slow time scales, indicative of Brownian rotation of polydisperse fibrils [73].

It is clear, that the behavior of CNF in shear flow is very complex and accurate predictions would require knowing the flexibility of individual fibrils, which is not fully understood and is probably highly dependent on the source materials and preparation steps.

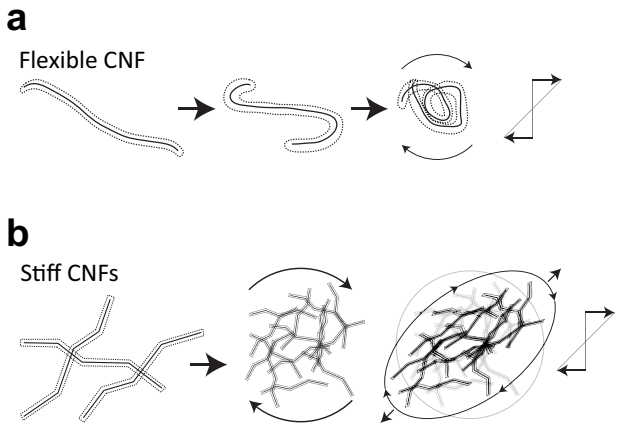

FIG. 11. Schematic illustration of hypothesized CNF behavior in shear flow. (a) Flexible CNF can potentially curl up in nearly spherical bundles and thus not be easily aligned. (b) Stiff CNF can potentially form larger bundles/flocks that are slightly stretched in the extensional direction of the shear flow (45° w.r.t. flow direction).

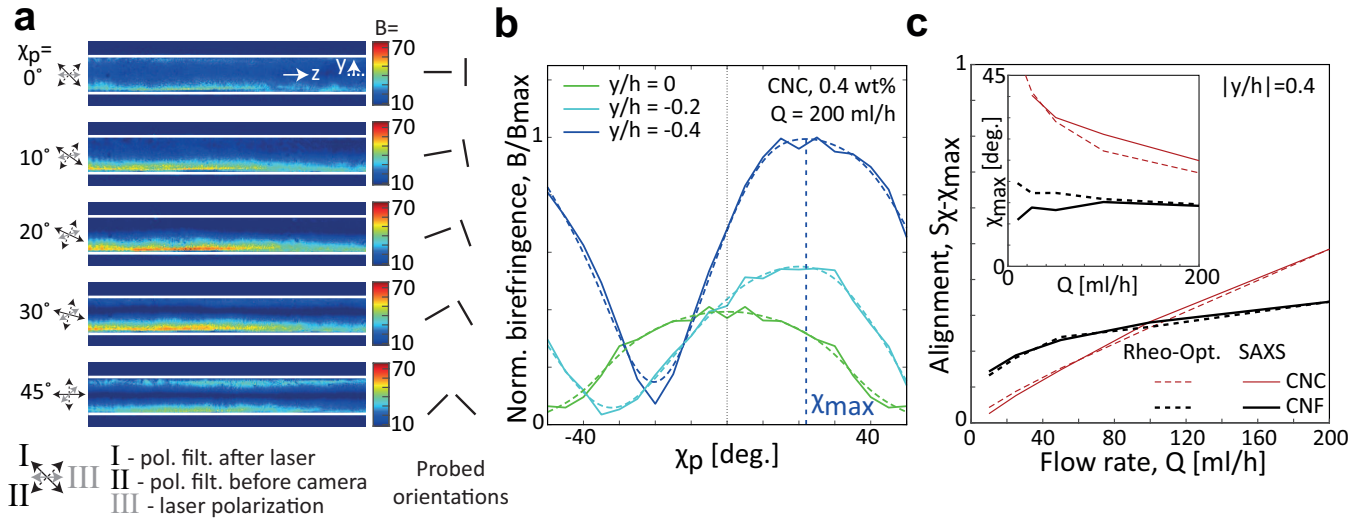

FIG. 12. Illustration of the rheo-optical experiments. (a) The optical setup (laser and polarization filters) is rotated with a probing angle χ_p and the average birefringence/alignment in different directions is estimated. (b) The normalized birefringence $B/B_{\max}$ at given probing angles χ_p are obtained by averaging the birefringence using assumption $B(y/h, \chi_p) = B(-y/h, -\chi_p)$. The dashed curves show the spline fits to obtain $\chi_{\max}$. (c) Alignment $S_{\chi-\chi_{max}}$ and angle $\chi_{\max}$ compared with SAXS are obtained by using $B \propto S_\chi$ and using the SAXS results at $Q = 200$ ml/h as reference.

V. A RHEO-OPTICAL APPROACH

Quick determination of the orientation distributions during flow typically rules out the usage of SAXS, which often requires the access to a synchrotron radiation facility or expensive lab-scale X-ray equipment. Since CNF and CNC dispersions are birefringent due to a crystalline structure along the particle principle axis, the orientation distribution can also be estimated by measuring the birefringence with rheo-optical techniques [27, 28]. However, state-of-the-art rheo-optical tools can also be expensive. Here, we will demonstrate a very simple and cheap setup that can be used for providing estimations of angle $\chi_{\max}$ and alignment $S_{\chi-\chi_{max}}$, similar to the work by Ober *et al.* [28].

The flow cell is placed between two cross-polarized linear polarization filters oriented $+45°$ and $-45°$ with respect to the flow direction (details in appendix E). A laser module with polarization parallel to the flow is used as the light source and the intensity I is simultaneously recorded with a camera. In this configuration, the square root of the recorded intensity I, called relative birefringence $B = \sqrt{I}$, is proportional to the orientation parameter $S_\phi = \langle \frac{3}{2}\cos^2\phi - \frac{1}{2} \rangle$, where ϕ is the 3D polar angle with respect to the flow direction [31, 73, 74] (see Fig. 1a). This technique is a measurement of the relative alignment along the flow direction, but it is only valid for small changes to birefringence in the sample and is not suitable for concentrated CNC systems. We therefore only measure on CNC and CNF at 0.4 wt%.

When rotating the optical setup with a certain angle χ_p, the relative degree of alignment $B_{\chi_p} \propto S_{\phi-\chi_p}$ is probed (see Fig. 12a). Observing the degree of birefringence at different probe angles χ_p close to the wall (Fig. 12b), it is seen that there is a maximum value at a certain probe angle similar to the highest probable angle found with the *in situ* SAXS experiments. This angle can be used as an estimation of $\chi_{\max}$ to compare with the previously obtained quantities. The rheo-optical experiments only give a relative measurement of the order parameter. Therefore, in order to compare it quantitatively with the SAXS results, a reference point is needed. In this study, the SAXS results of $S_{\chi-\chi_{\max}}$ at $Q = 200$ ml/h is used as a reference S_{ref} and the degree of alignment is given by $S_{\phi-\chi_{\max}} = (B_{\chi_{\max}}/B_{\text{ref}})S_{\text{ref}}$. Further assuming $S_\phi \approx S_\chi$, the results can be compared with the earlier SAXS-results.

The dashed curves in Fig. 12c show the results of the rheo-optical measurements of CNC and CNF at 0.4 wt%. Both for the CNF and CNC dispersions, the angle $\chi_{\max}$ can be very accurately predicted. The increase in alignment as a result of the flow rate is very accurately captured as long as there is one reference point with known alignment (here taken at $Q = 200$ ml/h) and assuming $S_\phi \approx S_\chi$. Since $\chi_{\max}$ and $S_{\chi-\chi_{max}}$ are indicative of particle shapes and interactions, this experiment could possibly provide a simple, cheap and quick way of estimating the constituents of a birefringent dispersion.

VI. CONCLUSIONS AND OUTLOOK

Flow-assisted assembly of nanostructured materials on an industrial scale has the potential to become a reality in a near future. In particular nanocellulosic materials, consisting of dispersed CNF and/or CNC, have

very promising properties in creating new biobased 1D materials (*e.g.* filaments for new textiles), 2D materials (*e.g.* barrier films, membranes for water purification) and even 3D-printed materials. By controlling the orientation distribution of these elongated particles during processing, the internal nanostructure and thus macroscopic material properties, such as mechanical strength/stiffness, can possibly be fine tuned.

Previous studies of flowing CNF/CNC dispersions have mainly focused on qualitative studies of alignment using rheo-optical techniques or only semi-quantitatively using SAXS comparing the alignment with integrated quantities such as Hermans orientation factor. There are, to our knowledge, no studies that take into consideration both the varying degree of shear rates and shear directions in a channel flow, as well as the non-axisymmetry of the orientation distribution function (ODF) caused by the planar deformation in a shear flow.

In this work, we have studied in detail the projected flow-induced orientation distributions of dispersed CNC and CNF in a square channel flow using scanning microbeam SAXS. For the CNC system, we demonstrated the difference in hydrodynamic alignment when the concentration is low (dilute), which in turn could be compared with simulations of non-interacting Brownian ellipsoids having similar dimensions. The results from simulations took into account different shear rates and shear directions and yielded a very similar projected ODF as obtained in the experiment. The good agreement between simulations and experiments indicates that the CNC dispersions at dilute concentrations indeed behave similarly to what can be expected from Brownian ellipsoids.

The main features used to compare ODFs was the highest probable projected angle $\chi_{\max}$ and degree of alignment in this direction $S_{\chi-\chi_{\max}}$. Generally, higher flow rates lead to stronger alignment at the walls as well as the ODF being more centered around the flow direction as $\chi_{\max} \to 0$ (instead of tilting towards the shear direction). At low flow rates, both semi-dilute dispersions of CNC and CNF show relatively high alignment, indicating that particle-particle interactions inhibit the effects of Brownian rotary diffusion and collectively respond to the shear. At high flow rates, the flow alignment seems limited and the ODF is seemingly reaching a point where it is independent of the flow rate but far from perfect alignment. For semi-dilute CNC dispersions, the likely reason is that the CNC move collectively in large ellipsoidal tactoids, which themselves have lower aspect ratios than individual particles and will thus spend less time aligned in flow direction. For semi-dilute CNF dispersions, the reason could be due to self-entanglement and/or fibrils forming bundles that rotate with local vorticity rather than aligning with the flow.

This study is the first quantitative investigation of CNF and CNC orientation distributions in a channel flow, which is the simplest process-relevant flow situation. As an outlook, it would be interesting to study different flow situations in the same way, where there is a combination of shear and extensional/compressional flows in converging or diverging channels. The study here indicates that the orientation distributions in shear-dominated flows are dependent on individual fibril sizes, shapes and properties. It would thus be interesting to study the influence of using different source materials (*e.g.* other types of biomass) and preparation methods (*e.g.* CNF oxidized through carboxymethylation). Additionally, improved numerical models including particle-particle interactions might reveal the keys for controlling the collective behavior of semi-dilute CNF and CNC dispersions. As demonstrated clearly through the numerical simulations, the ODF is very sensitive to the aspect ratio of the elongated nanoparticles. This opens up an intriguing idea of using this type of experiment as a measurement of particle shapes in dilute systems. We hypothesize that by collecting enough data of different systems (different sizes, aspect ratios and polydispersity), it might be possible using machine learning methods to link the evolution of the ODF at different flow rates to the most probable set of particle shapes.

As a final remark, we see this work as an important stepping stone towards using SAXS in combination with numerical simulations to study the *in situ* structural changes during bottom-up processing of nanostructured materials, which might stretch far beyond materials from cellulose.

VII. ACKNOWLEDGEMENTS

The authors acknowledge financial support from the National Science Foundation (DMR-1808690), the Alf de Ruvo Foundation (SCA) and the Hans Werthén Foundation (IVA). Experimental assistance by F. Camino, X. Huang, K. Johnson and M. Yang is also gratefully acknowledged. T.R. also acknowledges helpful discussions with F. Lundell, D. Söderberg, B. Mehlig and J. Einarsson as well as the fabrication of the flow cell by P. DiMatteo. A thank you is also directed to G. Terdik for the 3D-Directional-SSV method to illustrate 3D histograms in MATLAB.

The SAXS experiments were performed at the LiX beamline (16-ID) in NSLS-II at Brookhaven National Laboratory, USA. The LiX beamline is part of the Life Science Biomedical Technology Research resource, primarily supported by the National Institute of Health, National Institute of General Medical Sciences (NIGMS) under grant P41 GM111244, and by the DOE Office of Biological and Environmental Research under grant KP1605010, with additional support from NIH under grant S10 OD012331. As a National Synchrotron Light Source II facility resource at Brookhaven National Laboratory, work performed at the LSBR is supported in part by the U.S. Department of Energy, Office of Basic Energy Sciences Program under contract number DE-SC0012704.

Transmission electron microscopy (TEM) experiments

were performed at the Center of Functional Nanomaterials, Brookhaven National Laboratory. The Center for Functional Nanomaterials, which is a U.S. DOE Office of Science Facility, at Brookhaven National Laboratory under Contract No. DE-SC0012704.

Appendix A: Sample preparation

The TEMPO-oxidized cellulose nanofibrils (CNF) and cellulose nanocrystals (CNC) were purchased as aqueous slurries from the University of Maine Process Development Center.

The CNF slurry, produced from bleached wood pulp, contained 1.1 wt% of nanofibrils in water, where the TEMPO oxidation process had resulted in 1.5 mmol of carboxylate-groups (COO^-) per gram of dry material. The obtained slurry was diluted to the desired concentration, mixed and passed five times through a high pressure (200 bar) homogenizer. After subsequent microfiltration (40 μm) and overnight (>12h) ultrasonication, the CNF dispersion was assumed to be free of large aggregates. The final concentration was determined through the gravimetric analysis.

The CNC slurry also produced from wood pulp through sulfuric acid hydrolysis contained 12.1 wt% of nanocrystals in water. Through acid hydrolysis, the dispersion was stabilized with 0.3 mmol of sulfate-groups (OSO_3^{2-}) per gram of dry material. The obtained CNC slurry was diluted to the desired concentration with subsequent mixing prior to experiments.

The degree of interactions between the nanoparticles can be estimated using the crowding factor N, defined as [10, 75]:

$$N = \frac{2}{3}\Phi r_p^2 \tag{A1}$$

where, Φ is the volume fraction and r_p is the particle aspect ratio. The volume fraction can be estimated as the weight fraction multiplied with the ratio of densities between water (1000 kg/m^3) and cellulose (1500 kg/m^3). For CNF, the aspect ratios (estimated through TEM) are of $r_p = O(100)$, leading to a crowding factor of $N \approx 18$ at 0.4 wt%. For CNC, the aspect ratios are of $r_p = O(10)$, leading to crowding factors $N \approx 0.2, 0.5$ and 1.6 for concentrations $0.4, 1.1$ and 3.6 wt%, respectively. The average number of contacts points for an individual fiber [10] is given by $n_c = 3N/r_p$, so even if the CNC at 3.6 wt% has almost 10 times lower crowding factor than CNF at 0.4 wt%, they still experience approximately the same average number of contacts.

1. Fibril characterization with TEM

Transmission electron microscopy (TEM) experiments were performed using a JEOL JEM-1400 TEM instrument with a Ruby camera at the Center of Functional Nanomaterials, Brookhaven National Laboratory. For the measurements, the operating voltage was set to 120 kV. The CNF and CNC dispersions were diluted below 0.01 wt% and approximately 2.2 μL was dropped on a carbon-coated copper grid, followed by subsequent staining using 2 wt% of aqueous uranyl acetate solution in order to obtain sufficient contrast.

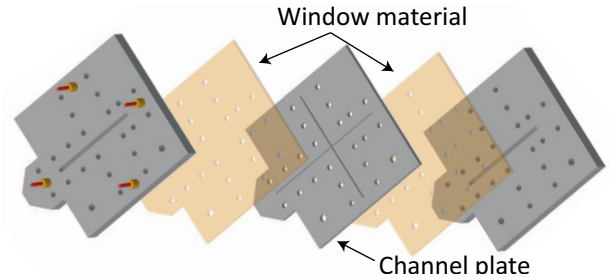

FIG. 13. Illustration of the flow cell, consisting of a channel plate, window material and thick aluminum plates.

Appendix B: Flow cell and setup

The experimental flow cell consisted of a four-channel crossing, where a core flow of CNF/CNC dispersion could be focused by two sheath flows of water (see Fig. 1a). Fig. 13 illustrates the assembly of the flow cell, which consists of: 1) a 1 mm aluminum channel plate where the flow-focusing channel is milled; 2) foils acting as window material and walls to the channel; the material is Kapton (DuPont, 200HN, each 51 μm thickness) for SAXS experiments and cyclic olefin polymer (COC, Tekni-plex 8007 X-04, each 150 μm thickness) for rheo-optical experiments; 3) 10 mm thick aluminum plates for mechanical stability and fluid distribution. The flow cell sandwich is assembled using 22 screws. The fluid distribution comprises two syringe pumps (NE-4000), one for the core flow and one (with two individual syringes) for the sheath flow. The flow rate Q is set to be the same on both syringe pumps and the outlet flow rate is thus $3Q$.

Appendix C: SAXS experiments

A schematic illustration of the experimental setup for the SAXS experiments is illustrated in Fig. 14a. The flow cell is mounted vertically with the main flow direction in the same direction as gravity. A traversing stage allows to direct the focused X-ray beam at a given y, z-position in the channel. The average orientation distribution functions in the square channel part upstream of the focusing section are obtained from scattering patterns at 9 lateral positions $y/h = -0.4, 0.3, \ldots, 0.4$ ($h = 1$ mm) and averaged over three downstream locations ($z/h = -0.5, -1.5$ and -2.5) as illustrated in Fig. 14a. The length of the channel between inlet and the

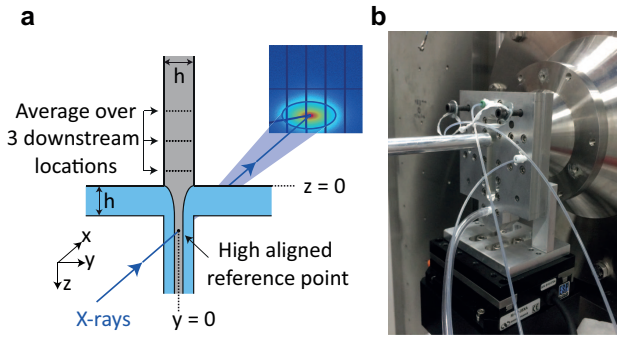

FIG. 14. (a) Schematic illustration of the setup for the SAXS experiments; (b) the actual flow cell on the translation stage at the LiX beamline, NSLS-II, Brookhaven National Laboratory.

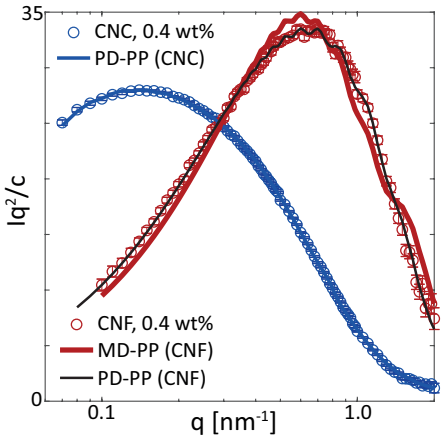

FIG. 15. Illustration of the fitting of the CNC and CNF isotropic scattering curves $I(q)$ using a monodisperse and polydisperse parallelepiped model (MD-PP and PD-PP).

measurement region is approximately 50 mm. The high aligned reference point is taken in the focusing region at $z/h = 1.5$ and $y = 0$ at a flow rate of $Q = 200$ ml/h. A photo of the actual setup at the LiX beamline (16-ID) at NSLS-II, Brookhaven National Laboratory is shown in Fig. 14b.

1. Isotropic $I(q)$ and fitting procedure

The isotropic scattering patterns were evaluated at the center of the channel upstream of the focusing region ($z/h = -2.5$, $y = 0$) at the lowest flow rate ($Q = 10$ ml/h). The scattering diffractogram $I(q, \chi)$ was averaged over all projected angles χ to form the isotropic curves $I(q)$ in Fig. 1c in the main manuscript. The data at 0.4 wt.% was used as the form factor for both CNF and CNC to determine the approximate cross-sectional dimensions through fitting using SasView v4.1.2.

For CNF, the $I(q)$-curve was fitted using a monodisperse parallelepiped model with length assumed to be $L = 1000$ nm, which is large enough to not have any significant effect on the scattering within the q-range. The resulting fit providing cross-sectional dimensions of 5.6×2.0 nm^2 is illustrated in Fig. 15. The fit can be improved by including polydispersity (black curve in Fig. 15) or using more complicated models, but it was determined that a simpler model is more reasonable to capture the mean dimensions accurately.

For CNC, the $I(q)$-curve was fitted using a polydisperse parallelepiped model with length fixed to $L = 200$ nm, similar to the length in the TEM images. Polydispersity was included as the monodisperse model was not able to capture the important features in the scattering pattern. Polydispersity to both width and height was included using an assumption of a lognormal distribution of each dimension. The resulting fit providing mean cross-sectional dimensions of 30.8×3.5 nm^2 (standard deviations 20.2 nm and 1.5 nm, respectively) is illustrated in Fig. 15.

Appendix D: Numerical simulations

The numerical simulations to obtain the orientation distribution of spheroidal particles in channel flow were carried out based on the method by Almondo *et al.* [39], which describes the Brownian rotation of a single ellipsoid in an unbounded linear flow field that can be represented by a velocity gradient matrix $\mathbb{J}$. The simulations were implemented in MATLAB R2018b.

The velocity profile of a fully developed laminar flow through a square channel with side $h = 1$ mm and volumetric flow rate Q was obtained from Spiga and Morini [32]. The cross section is discretized into 10×10 equally sized cells, in which the average spatial velocity derivatives were estimated, and the velocity gradient matrix $\mathbb{J}$ could be defined in each cell. Note that all derivatives in the flow (z) direction are zero, as well as the velocity components u_x and u_y. The only non-zero velocity gradients are du_z/dx and du_z/dy. The shear rate in each cell was defined by $\dot{\gamma} = \sqrt{(du_z/dx)^2 + (du_z/dy)^2}$. The minor semi-axis of each spheroid was chosen to be $b = 10/2$ nm$= 5$ nm. Depending on the chosen aspect ratio r_p, the major semi-axis of the spheroid was determined as $a = b/r_p$. The Peclet number, Pe, is defined as $Pe = \dot{\gamma}\mu V_p/(k_B T)$, where $\mu = 10^{-3}$ Pa s (water), $T = 293$ K (room temperature), k_B is the Boltzmann constant and $V_p = 4\pi ab^2/3$ is the volume of the spheroid.

Given the chosen aspect ratio r_p and Peclet number Pe in one cell, a spheroid was sampled with a random initial orientation. The spheroid was simulated for two rotational periods $2T_J$ defined at $Pe = 0$ by Jeffery [33] as $T_J = 2\pi(r_p + r_p^{-1})/\dot{\gamma}$. The time step δt was chosen to be inversely proportional to $\dot{\gamma}$ (higher shear rate leads to smaller time step) and linearly proportional to r_p (as the Jeffery-period increases almost linearly with r_p). As a compromise of accuracy and computational time, a time

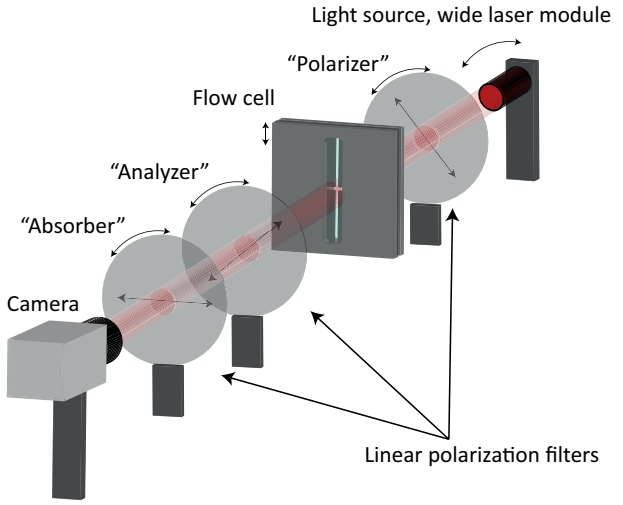

FIG. 16. Schematic illustration of the optical setup for the rheo-optical experiments.

step of $\delta t = r_p/(5000\dot{\gamma})$ was chosen. The procedure was repeated for $N_p = 50$ particles in all of the 100 cells.

The midpoint heights of the simulated cells were given by $y/h = 0.45, 0.4, \ldots, -0.45$. To determine the 3D orientation data at a certain height $y/h = 0.4, 0.3, \ldots, -0.4$, the combined data from all adjacent cells in the viewing (x) direction (a total of 20 cells) was considered (Fig. 4b). The time series of all the orientations of all particles in these cells were combined together. From the total combined data set at $T_J < t < 2T_J$, consisting of ≈ 30 million individual orientations at a statistically assumed steady state (statistics were found not to vary in time), 500000 individual orientations were randomly chosen to form the total 3D orientation distribution function (ODF) in the viewing direction. The orientation of a particle was described by a unit vector $\boldsymbol{p} = (p_x, p_y, p_z)$ in the direction of the particle major axis. From the 3D ODF, we could define the order parameter $S_\phi = \left\langle \frac{3}{2}\cos^2\phi - \frac{1}{2} \right\rangle$, where ϕ is the spherical polar angle between $\boldsymbol{p}$ and the z-axis and the brackets denote an ensemble average of fibrils.

From the chosen set of particle orientations, the projected angle was calculated as $\chi = \text{atan2}(p_y, p_z)$, compressed to the range $\chi \in [-90°, 90°]$ using the fact that $\chi = 90° + \chi_0$ is equivalent to $\chi = -90° + \chi_0$ for an arbitrary χ_0 (and $\chi = -90° - \chi_0$ is equivalent to $\chi = 90° - \chi_0$). The histogram of the 500000 values of χ was normalized to create the 2D orientation distribution function Ψ_χ of the projected angle χ at a given channel height y, flow rate Q and aspect ratio r_p. The procedure was repeated for aspect ratios $r_p = 10, 15, 25$ and 50 and for flow rates $Q = 5, 10, 25, 50, 100$ and 200 ml/h. All ODFs from the numerical simulations are provided as supplementary information [76].

Appendix E: Rheo-optical experiments

Fig. 16 illustrates the optical setup of the rheo-optcial experiments. The flow cell was placed between two linear polarization filters mounted on precision rotation stages with manual control of polarization direction. The Kapton films were replaced by 150 μm thick COC films (Tekni-plex 8007 X-04) with very low birefringence. The channel was illuminated by a wide laser module ($\lambda = 660$ nm, spot size ≈ 10 mm diameter), which was also mounted to be allowed to rotate. In the standard configuration, the laser light, polarized in the flow direction, was travelling through the first (polarizer) filter, polarized $+45°$ to the flow direction, through the flow cell and then through a second (analyzer) filter, polarized $-45°$ to the flow direction. In order to not saturate the pixel values on the camera at the lowest exposure time, an additional polarization (absorber) filter was placed directly after the analyzer (rotating together with analyzer) to reduce the intensity. The transmitted light was recorded by a CCD camera (Mako U-029B, Allied Vision). In this configuration, the transmitted light intensity is equal to [77]:

$$I = I_0 \sin^2(\Delta\gamma), \tag{E1}$$

where $\Delta\gamma = (2\pi d/\lambda)\Delta n$. Here, d is the sample thickness, I_0 is an unknown constant related to the laser intensity, λ is the laser wavelength and Δn is the difference between the refractive indices in flow and cross-flow directions, *i.e.* the birefringence of the material caused by CNC/CNF alignment in the flow (or cross-flow) direction. For the CNF/CNC dispersions at 0.4wt%, the phase shift $\Delta\gamma$ can be assumed small and the intensity becomes directly proportional to the square of birefringence $I \propto (\Delta n)^2$. Furthermore, it is known by Van Gurp [74] that the birefringence of the material is proportional to the Herman orientation parameter of the fibrils $S_\phi = \langle \frac{3}{2}\cos^2\phi - \frac{1}{2} \rangle$. As S_ϕ is directly proportional to Δn, a relative relationship can be written as $S_\phi = (S_{\phi,\text{ref}}/\sqrt{I_\text{ref}})\sqrt{I}$, where the exact value of S_ϕ only can be known by relating it to some reference data. For each separate sample, we define the reference at $Q = 200$ ml/h, where $S_{\phi,\text{ref}}$ is estimated from SAXS (assuming $S_\phi \approx S_\chi$) and I_ref is the intensity at the same position and flow rate.

The measurements were done by recording the intensity for different probing angles $\chi_p = 45°, 40°, \ldots, -45°$, by rotating the entire optical setup (laser + polarizer + analyzer + absorber) from the standard configuration with the same angle. The intensity was further adjusted using the assumption that the maximum $S_{\phi-\chi_p}$ is equal regardless of positive or negative y/h. This allowed us to map out $S_{\phi-\chi_p}$ in the entire channel, which is defined as the 3D alignment around an axis in the viewing plane with angle χ_p to the flow direction. The angle χ_max is

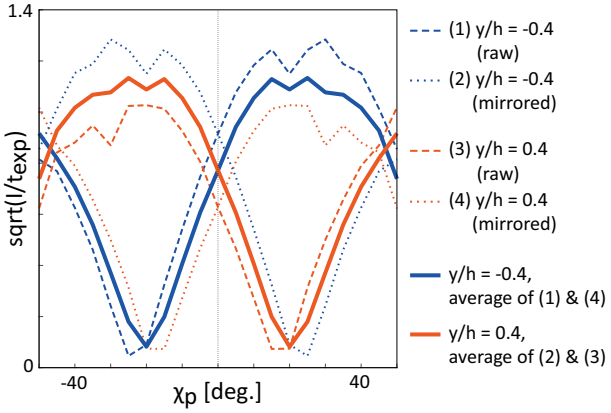

FIG. 17. Illustration of how the birefringence curves are obtained in the rheo-optical experiments; the final curves are taken as the average of the raw curve at a given position y (dashed) and the mirrored curve at position $-y$ (dotted).

defined at a certain channel region as the χ_p that maximizes $S_{\phi-\chi_p}$ in the set of pixels included in region.

Fig. 17 illustrates the procedure to obtain the birefringence curves from the rheo-optical experiments. The intensity I scaled with the exposure time t_{exp} is evaluated at a certain y-position in the channel for various probing angles χ_p (filters and laser rotated with this angle). This results in the two dashed curves for positions $y/h = -0.4$ (blue) and $y/h = 0.4$ (red). For a perfect optical setup, these two curves would just mirror each other, since the flow is symmetric around the $y = 0$ plane. To correct this, the final curve at $y/h = -0.4$ is taken as the average of the raw curve at $y/h = -0.4$ and the mirrored curve from $y/h = 0.4$, and vice versa. This forces the two curves to be perfect mirror images of each other as illustrated in the figure. All birefringence curves from the rheo-optical experiments are provided as supplementary information [76].

[1] U. G. Wegst, H. Bai, E. Saiz, A. P. Tomsia, and R. O. Ritchie, Bioinspired Structural Materials, Nat. Mater. **14**, 23 (2015).

[2] G. M. Whitesides, J. K. Kriebel, and B. T. Mayers, Self-assembly and Nanostructured Materials, in *Nanoscale Assembly* (Springer, 2005) pp. 217–239.

[3] S. Ling, D. L. Kaplan, and M. J. Buehler, Nanofibrils in Nature and Materials Engineering, Nat. Rev. Mater. **3**, 18016 (2018).

[4] L. Chen, Y. He, S. Chai, H. Qiang, F. Chen, and Q. Fu, Toward High Performance Graphene Fibers, Nanoscale **5**, 5809 (2013).

[5] Y.-Z. Long, M. Yu, B. Sun, C.-Z. Gu, and Z. Fan, Recent Advances in Large-scale Assembly of Semiconducting Inorganic Nanowires and Nanofibers for Electronics, Sensors and Photovoltaics, Chem. Soc. Rev. **41**, 4560 (2012).

[6] K. Håkansson, *Orientation of Elongated, Macro and Nano-Sized Particles in Macroscopic Flows*, Ph.D. thesis, Royal Institute of Technology (KTH) (2014).

[7] S. Hooshmand, Y. Aitomäki, N. Norberg, A. P. Mathew, and K. Oksman, Dry-Spun Single-Filament Fibers Comprising Solely Cellulose Nanofibers from Bioresidue, ACS Appl. Mater. Interfaces **7**, 13022 (2015).

[8] D. J. Finn, M. Lotya, and J. N. Coleman, Inkjet Printing of Silver Nanowire Networks, ACS Appl. Mater. Inter. **7**, 9254 (2015).

[9] A. Kamada, N. Mittal, L. D. Söderberg, T. Ingverud, W. Ohm, S. V. Roth, F. Lundell, and C. Lendel, Flow-Assisted Assembly of Nanostructured Protein Microfibers, Proc. Natl. Acad. Sci. **114**, 1232 (2017).

[10] N. Mittal, F. Ansari, K. Gowda. V, C. Brouzet, P. Chen, P. T. Larsson, S. V. Roth, F. Lundell, L. Wågberg, N. A. Kotov, and L. D. Söderberg, Multiscale Control of Nanocellulose Assembly: Transferring Remarkable Nanoscale Fibril Mechanics to Macroscale Fibers, ACS Nano **12**, 6378 (2018).

[11] M. Henriksson, L. A. Berglund, P. Isaksson, T. Lindstrom, and T. Nishino, Cellulose Nanopaper Structures of High Toughness, Biomacromolecules **9**, 1579 (2008).

[12] R. Allen, G. G. Fuller, and Z. Bao, Aligned SWNT Films from Low-Yield Stress Gels and Their Transparent Electrode Performance, ACS Appl. Mater. Inter. **5**, 7244 (2013).

[13] L.-P. Simoneau, J. Villeneuve, C. M. Aguirre, R. Martel, P. Desjardins, and A. Rochefort, Influence of Statistical Distributions on the Electrical Properties of Disordered and Aligned Carbon Nanotube Networks, J. Appl. Phys. **114**, 114312 (2013).

[14] A. Mautner, K.-Y. Lee, P. Lahtinen, M. Hakalahti, T. Tammelin, K. Li, and A. Bismarck, Nanopapers for Organic Solvent Nanofiltration, Chem. Commun. **50**, 5778 (2014).

[15] H. Voisin, L. Bergström, P. Liu, and A. Mathew, Nanocellulose-Based Materials for Water Purification, Nanomaterials **7**, 57 (2017).

[16] K. M. Håkansson, I. C. Henriksson, C. de la Peña Vázquez, V. Kuzmenko, K. Markstedt, P. Enoksson, and P. Gatenholm, Solidification of 3D Printed Nanofibril Hydrogels into Functional 3D Cellulose Structures, Adv. Mater. Technol. **1**, 1600096 (2016).

[17] G. Siqueira, D. Kokkinis, R. Libanori, M. K. Hausmann, A. S. Gladman, A. Neels, P. Tingaut, T. Zimmermann, J. A. Lewis, and A. R. Studart, Cellulose Nanocrystal Inks for 3D Printing of Textured Cellular Architectures, Adv. Funct. Mater. **27**, 1604619 (2017).

[18] M. K. Hausmann, P. A. Rühs, G. Siqueira, J. Läuger, R. Libanori, T. Zimmermann, and A. R. Studart, Dynamics of Cellulose Nanocrystal Alignment during 3D Printing, ACS Nano **12**, 6926 (2018).

[19] P. L. Frattini and G. G. Fuller, Rheo-Optical Studies of the Effect of Weak Brownian Rotations in Sheared Suspensions, J. Fluid Mech. **168**, 119 (1986).

[20] L. M. Walker and N. J. Wagner, SANS Analysis of the Molecular Order in Poly (γ-benzyl l-glutamate)/Deuterated Dimethylformamide (PBLG/d-DMF) under Shear and During Relaxation, Macromolecules **29**, 2298 (1996).

[21] J. Vermant, H. Yang, and G. Fuller, Rheooptical De-

termination of Aspect Ratio and Polydispersity of Nonspherical Particles, AIChE J. **47**, 790 (2001).
[22] C. R. López-Barrón, A. K. Gurnon, A. P. Eberle, L. Porcar, and N. J. Wagner, Microstructural Evolution of a Model, Shear-Banding Micellar Solution During Shear Startup and Cessation, Phys. Rev. E **89**, 042301 (2014).
[23] J. K. Riley, J. J. Richards, N. J. Wagner, and P. D. Butler, Branching and Alignment in Reverse Worm-Like Micelles Studied with Simultaneous Dielectric Spectroscopy and RheoSANS, Soft Matter **14**, 5344 (2018).
[24] S. Pujari, S. S. Rahatekar, J. W. Gilman, K. K. Koziol, A. H. Windle, and W. R. Burghardt, Orientation Dynamics in Multiwalled Carbon Nanotube Dispersions under Shear Flow, J. Chem. Phys. **130**, 214903 (2009).
[25] S. Pujari, S. Rahatekar, J. W. Gilman, K. K. Koziol, A. H. Windle, and W. R. Burghardt, Shear-Induced Anisotropy of Concentrated Multiwalled Carbon Nanotube Suspensions using X-Ray Scattering, J. Rheol. **55**, 1033 (2011).
[26] S. J. Johnson, P. L. Frattini, and G. G. Fuller, Simultaneous Dichroism and Birefringence Measurements of Dilute Colloidal Suspensions in Transient Shear Flow, J. Colloid Interf. Sci. **104**, 440 (1985).
[27] G. G. Fuller, Optical Rheometry, Annu. Rev. Fluid Mech. **22**, 387 (1990).
[28] T. J. Ober, J. Soulages, and G. H. McKinley, Spatially Resolved Quantitative Rheo-Optics of Complex Fluids in a Microfluidic Device, J. Rheol. **55**, 1127 (2011).
[29] T. Saarinen, S. Haavisto, A. Sorvari, J. Salmela, and J. Seppälä, The Effect of Wall Depletion on the Rheology of Microfibrillated Cellulose Water Suspensions by Optical Coherence Tomography, Cellulose **21**, 1261 (2014).
[30] K. Gowda V., C. Brouzet, T. Lefranc, L. D. Söderberg, and F. Lundell, Effective Interfacial Tension in Flow-Focusing of Colloidal Dispersions: 3-D Numerical Simulations and Experiments, J. Fluid Mech. **876**, 1052 (2019).
[31] T. Rosén, N. Mittal, S. V. Roth, P. Zhang, L. D. Söderberg, and F. Lundell, Dynamic Characterization of Cellulose Nanofibrils in Sheared and Extended Semi-Dilute Dispersions, arXiv preprint arXiv:1801.07558 (2018).
[32] M. Spiga and G. Morini, A Symmetric Solution for Velocity Profile in Laminar Flow through Rectangular Ducts, Int. Commun. Heat Mass Transfer **21**, 469 (1994).
[33] G. B. Jeffery, The Motion of Ellipsoidal Particles Immersed in a Viscous Fluid, Proc. R. Soc. London, Ser. A **102**, 161 (1922).
[34] L. Leal and E. Hinch, The Effect of Weak Brownian Rotations on Particles in Shear Flow, J. Fluid Mech. **46**, 685 (1971).
[35] E. Hinch and L. Leal, The Effect of Brownian Motion on the Rheological Properties of a Suspension of Nonspherical Particles, J. Fluid Mech. **52**, 683 (1972).
[36] E. Hinch and L. Leal, Constitutive Equations in Suspension Mechanics. Part 1. General Formulation, J. Fluid Mech. **71**, 481 (1975).
[37] E. Hinch and L. Leal, Constitutive Equations in Suspension Mechanics. Part 2. Approximate Forms for a Suspension of Rigid Particles Affected by Brownian Rotations, J. Fluid Mech. **76**, 187 (1976).
[38] A. L. Yarin, O. Gottlieb, and I. V. Roisman, Chaotic Rotation of Triaxial Ellipsoids in Simple Shear Flow, J. Fluid. Mech. **340**, 83 (1997).
[39] G. Almondo, J. Einarsson, J. Angilella, and B. Mehlig, Intrinsic Viscosity of a Suspension of Weakly Brownian Ellipsoids In Shear, Phys. Rev. Fluids **3**, 064307 (2018).
[40] M. Doi and S. F. Edwards, *The Theory of Polymer Dynamics* (Oxford university press, 1986).
[41] K. M. Håkansson, F. Lundell, L. Prahl-Wittberg, and L. D. Söderberg, Nanofibril alignment in flow focusing: Measurements and calculations, J. Phys. Chem. B **120**, 6674 (2016).
[42] N. Fakhri, F. C. MacKintosh, B. Lounis, L. Cognet, and M. Pasquali, Brownian Motion of Stiff Filaments in a Crowded Environment, Science **330**, 1804 (2010).
[43] C. Brouzet, N. Mittal, F. Lundell, and D. Söderberg, Characterizing the Orientational and Network Dynamics of Polydisperse Nanofibres at the Nanoscale, Macromolecules **52**, 2286 (2019).
[44] K. M. Håkansson, A. B. Fall, F. Lundell, S. Yu, C. Krywka, S. V. Roth, G. Santoro, M. Kvick, L. P. Wittberg, L. Wågberg, *et al.*, Hydrodynamic Alignment and Assembly of Nanofibrils Resulting in Strong Cellulose Filaments, Nat. Commun. **5**, 4018 (2014).
[45] T. Rosén, C. Brouzet, S. V. Roth, F. Lundell, and L. D. Söderberg, Three-Dimensional Orientation of Nanofibrils in Axially Symmetric Systems Using Small-Angle X-ray Scattering, J. Phys. Chem. C **122**, 6889 (2018).
[46] S. J. Eichhorn, A. Dufresne, M. Aranguren, N. Marcovich, J. Capadona, S. Rowan, C. Weder, W. Thielemans, M. Roman, S. Renneckar, *et al.*, Current International Research into Cellulose Nanofibres and Nanocomposites, J. Mater. Sci. **45**, 1 (2010).
[47] D. Klemm, E. D. Cranston, D. Fischer, M. Gama, S. A. Kedzior, D. Kralisch, F. Kramer, T. Kondo, T. Lindström, S. Nietzsche, K. Petzold-Welcke, and F. Rauchfuss, Nanocellulose as a Natural Source for Groundbreaking Applications in Materials Science: Today's State, Mater. Today **21**, 720 (2018).
[48] R. M. Parker, G. Guidetti, C. A. Williams, T. Zhao, A. Narkevicius, S. Vignolini, and B. Frka-Petesic, The Self-Assembly of Cellulose Nanocrystals: Hierarchical Design of Visual Appearance, Adv. Mater. **30**, 1704477 (2018).
[49] M. J. Lundahl, V. Klar, L. Wang, M. Ago, and O. J. Rojas, Spinning of Cellulose Nanofibrils into Filaments: A Review, Ind. Eng. Chem. Res. **56**, 8 (2016).
[50] T. Pfohl, A. Otten, S. Köster, R. Dootz, B. Struth, and H. M. Evans, Highly Packed and Oriented DNA Mesophases Identified using In Situ Microfluidic X-ray Microdiffraction, Biomacromolecules **8**, 2167 (2007).
[51] M. Trebbin, D. Steinhauser, J. Perlich, A. Buffet, S. V. Roth, W. Zimmermann, J. Thiele, and S. Förster, Anisotropic Particles Align Perpendicular to the Flow Direction in Narrow Microchannels, Proc. Natl. Acad. Sci. **110**, 6706 (2013).
[52] B. F. Silva, M. Zepeda-Rosales, N. Venkateswaran, B. J. Fletcher, L. G. Carter, T. Matsui, T. M. Weiss, J. Han, Y. Li, U. Olsson, and C. R. Safinya, Nematic Director Reorientation at Solid and Liquid Interfaces under Flow: SAXS Studies in a Microfluidic Device, Langmuir **31**, 4361 (2014).
[53] V. Lutz-Bueno, J. Zhao, R. Mezzenga, T. Pfohl, P. Fischer, and M. Liebi, Scanning-SAXS of Microfluidic Flows: Nanostructural Mapping of Soft Matter, Lab Chip **16**, 4028 (2016).
[54] M. Schlenk, E. Hofmann, S. Seibt, S. Rosenfeldt,

L. Schrack, M. Drechsler, A. Rothkirch, W. Ohm, J. Breu, S. Gekle, and S. Förster, Parallel and Perpendicular Alignment of Anisotropic Particles in Free Liquid Microjets and Emerging Microdroplets, Langmuir **34**, 4843 (2018).

[55] J.-F. Revol, H. Bradford, J. Giasson, R. Marchessault, and D. Gray, Helicoidal Self-Ordering of Cellulose Microfibrils in Aqueous Suspension, Int. J. Biol. Macromol. **14**, 170 (1992).

[56] P.-X. Wang, W. Y. Hamad, and M. J. MacLachlan, Structure and Transformation of Tactoids in Cellulose Nanocrystal Suspensions, Nat. Commun. **7**, 11515 (2016).

[57] K. J. De France, K. G. Yager, T. Hoare, and E. D. Cranston, Cooperative Ordering and Kinetics of Cellulose Nanocrystal Alignment in a Magnetic Field, Langmuir **32**, 7564 (2016).

[58] Y. Mao, M. Bleuel, Y. Lyu, X. Zhang, D. Henderson, H. Wang, and R. M. Briber, Phase Separation and Stack Alignment in Aqueous Cellulose Nanocrystal Suspension under Weak Magnetic Field, Langmuir **34**, 8042 (2018).

[59] C. Schütz, M. Agthe, A. B. Fall, K. Gordeyeva, V. Guccini, M. Salajkova, T. S. Plivelic, J. P. Lagerwall, G. Salazar-Alvarez, and L. Bergström, Rod Packing in Chiral Nematic Cellulose Nanocrystal Dispersions Studied by Small-Angle X-ray Scattering and Laser Diffraction, Langmuir **31**, 6507 (2015).

[60] Y. Liu, C. Schütz, G. Salazar-Alvarez, and L. Bergström, Assembly, Gelation, and Helicoidal Consolidation of Nanocellulose Dispersions, Langmuir **35**, 3600 (2019).

[61] B. D. Leahy, D. L. Koch, and I. Cohen, The Effect of Shear Flow on the Rotational Diffusion of a Single Axisymmetric Particle, J. Fluid Mech. **772**, 42 (2015).

[62] D. Palanisamy and W. K. den Otter, Intrinsic Viscosities of Non-spherical Colloids by Brownian Dynamics Simulations, J. Chem. Phys. **151**, 184902 (2019).

[63] A. Naderi, T. Lindström, and J. Sundström, Carboxymethylated Nanofibrillated Cellulose: Rheological Studies, Cellulose **21**, 1561 (2014).

[64] Y. Xu, A. D. Atrens, and J. R. Stokes, "Liquid, Gel and Soft Glass" Phase Transitions and Rheology of Nanocrystalline Cellulose Suspensions as a Function of Concentration and Salinity, Soft Matter **14**, 1953 (2018).

[65] B. D. Leahy, X. Cheng, D. C. Ong, C. Liddell-Watson, and I. Cohen, Enhancing Rotational Diffusion using Oscillatory Shear, Phys. Rev. Lett. **110**, 228301 (2013).

[66] D. G. Gray and X. Mu, Twist–Bend stage in the Relaxation of Sheared Chiral Nematic Suspensions of Cellulose Nanocrystals, ACS Omega **1**, 212 (2016).

[67] S. B. Lindström and T. Uesaka, Simulation of the Motion of Flexible Fibers in Viscous Fluid Flow, Phys. Fluids **19**, 113307 (2007).

[68] O. Forgacs and S. Mason, Particle Motions in Sheared Suspensions: X. Orbits of Flexible Threadlike Particles, J. Colloid Sci. **14**, 473 (1959).

[69] D. E. Smith, H. P. Babcock, and S. Chu, Single-Polymer Dynamics in Steady Shear Flow, Science **283**, 1724 (1999).

[70] C. Pozrikidis, Effect of Membrane Bending Stiffness on the Deformation of Capsules in Simple Shear Flow, J. Fluid Mech. **440**, 269 (2001).

[71] Y. Sui, Y. Chew, P. Roy, Y. Cheng, and H. Low, Dynamic Motion of Red Blood Cells in Simple Shear Flow, Phys. Fluids **20**, 112106 (2008).

[72] F. Martoïa, P. Dumont, L. Orgéas, M. Belgacem, and J.-L. Putaux, Micro-Mechanics of Electrostatically Stabilized Suspensions of Cellulose Nanofibrils under Steady State Shear Flow, Soft Matter **12**, 1721 (2016).

[73] C. Brouzet, N. Mittal, L. D. Söderberg, and F. Lundell, Size-Dependent Orientational Dynamics of Brownian Nanorods, ACS Macro Lett. **7**, 1022 (2018).

[74] M. Van Gurp, The Use of Rotation Matrices in the Mathematical Description of Molecular Orientations in Polymers, Colloid Polym. Sci. **273**, 607 (1995).

[75] L. Geng, N. Mittal, C. Zhan, F. Ansari, P. R. Sharma, X. Peng, B. S. Hsiao, and L. D. Söderberg, Understanding the Mechanistic Behavior of Highly Charged Cellulose Nanofibers in Aqueous Systems, Macromolecules **51**, 1498 (2018).

[76] See Supplemental Material at [URL will be inserted by publisher] for more details.

[77] E. Hecht, *Optics*, 4th ed. (Addison-Wesley, 2002).